Impacts of Hurricane Maria on Land and Convection Modification Over Puerto Rico

N. Hosannah[1] [ORCID], **P. Ramamurthy[2]** [ORCID], **J. Marti[3]**, **J. Munoz[3]** [ORCID], and **J. E. González[2]**

[1]Department of Mathematics, Engineering, and Computer Science, LaGuardia Community College, Long Island City, NY, USA, [2]NOAA CREST and Department of Mechanical Engineering, The City College of New York, New York, NY, USA, [3]Department of Civil Engineering, University of Puerto Rico Mayaguez, Mayagüez, PR, USA

Abstract Hurricane Maria drastically altered the landscape across the island of Puerto Rico. This article investigates modifications to surface-atmospheric interactions due to Hurricane Maria induced land damage and the associated impacts on local convective dynamics. Herein, we employed LANDSAT-8 image mosaics to quantify the hurricane induced land modification. Results of the analysis indicate that the island suffered significant forest damage—much of which registered as a 28.35% increase in barren land and a 10.85% increase in pasture. Smaller changes included a decrease in cultivated agricultural land cover by 0.76%, along with wetland and water increases of 0.62% and 0.25%, respectively. Pre and postMaria land classifications were then assimilated into the Regional Atmospheric Modeling System cloud resolving model for the simulation of the June 23 to July 2, 2018 period under two land conditions. Results of the numerical experiments indicate that surface to atmosphere interactions were significantly modified when the land cover was altered, and that the highest deviations between pre and postMaria convection occurred over elevated areas with extreme hurricane induced land changes, such as the Cordillera Central mountain range and the El Yunque rainforest.

1. Introduction

The island of Puerto Rico is home to over 3.5 million people who live under the threat of hurricanes during the late rainfall season (July to November). Hurricanes can cause severe flooding, extreme winds, and storm surge which lead to catastrophic loss of life, extreme damage to critical infrastructure, erosion, and defoliation (Tanner et al., 1991). Examples include Hurricanes Jeanne and Georges, which caused significant damage across Puerto Rico (Bennett & Mojica, 2008; Lawrence & Cobb, 2005). While the frequency of hurricane occurrence has decreased in recent decades, storms with the intensity of Jeanne and Georges are occurring more frequently due to global warming (Kang & Elsner, 2015), large scale changes in climate (Knutson et al., 2013, 2019) and El Niño Southern Oscillation (ENSO) modifications (Tang & Neelin, 2004).

In September 2017, Puerto Rico was hit by Hurricanes Irma and Maria. Hurricane Irma brushed the northern part of the island and caused flooding in the capital city of San Juan (home to nearly half a million people), whereas the eye of Hurricane Maria traveled diagonally across the island from the southeast to the northwest. Maria was the strongest hurricane to make landfall on Puerto Rico since 1928, with wind speeds exceeding 250 km h^{-1}, eclipsing Jeanne and Georges. Maria caused over 2,975 casualties (Kishore et al., 2018; Milken Institute, 2018) in addition to catastrophic wind and flood damage—which crippled the power grid (Schladebeck, 2017) and severely damaged roadways—thereby suspending evacuation efforts and the movement of supplies. The extensive damage to the island's land cover (Flynn et al., 2018) can alter local land-atmosphere interactions and the general climatology of the island.

Puerto Rico's rainfall climatology is characterized by a wet season occurring between April and October, and a dry season occurring between November and March. The wet season is bimodal, with a period of reduced rainfall during June to July known as the midsummer drought (Angeles et al., 2010; D. W. Gamble & Curtis, 2008; D. W. Gamble et al., 2008). The wet season accounts for 79% of the island's rainfall, with the summer months scaffolding the most convectively active period. As a result of this, the authors monitored surface-atmospheric conditions during late June and early July 2018 to study the impacts of Hurricane Maria induced land modification on convective storm events in Puerto Rico via the Rapid Response—Convection, Aerosol, and Synoptic-Effects in the Tropics (RAPID-CAST) field campaign (described in Section 2.1).

Validation: N. Hosannah
Visualization: N. Hosannah, J. Marti, J. Munoz
Writing – original draft: N. Hosannah, P. Ramamurthy, J. Munoz
Writing – review & editing: N. Hosannah, P. Ramamurthy

Figure 1 shows the 31-year (1990–2020) precipitation climatology calculated from monthly Global Historical Climate Network (GHCN) station data (locations are listed in Table S1) for June and July and the 2018 departure from climatology for both months—attained by subtracting the climatological values from the 2018 totals.

The June 2018 anomaly suggests that Puerto Rico experienced rainfall deficits exceeding 100 mm at several locations across the island, with surpluses ranging from 10 to 58 mm at 7 of the 32 stations with June 2018 data (41 stations total) July 2018 data indicates further reductions particularly on the west coast along the 18.2°N latitude, where GHCN data indicates a rainfall deficit of −266 mm. Four out of the 27 stations with July 2018 data indicate surpluses ranging from 18 to 64 mm. Here we investigate how surface atmospheric interactions which impact local rainfall production may have been altered as a result of Hurricane Maria induced damage.

1.1. Large and Local Scale Impacts on Caribbean Climate

Puerto Rico's climate is regulated by interactions between large scale systems such as the North Atlantic Oscillation (NAO), Saharan Dust advection and African easterly waves, and local island effects (Comarazamy
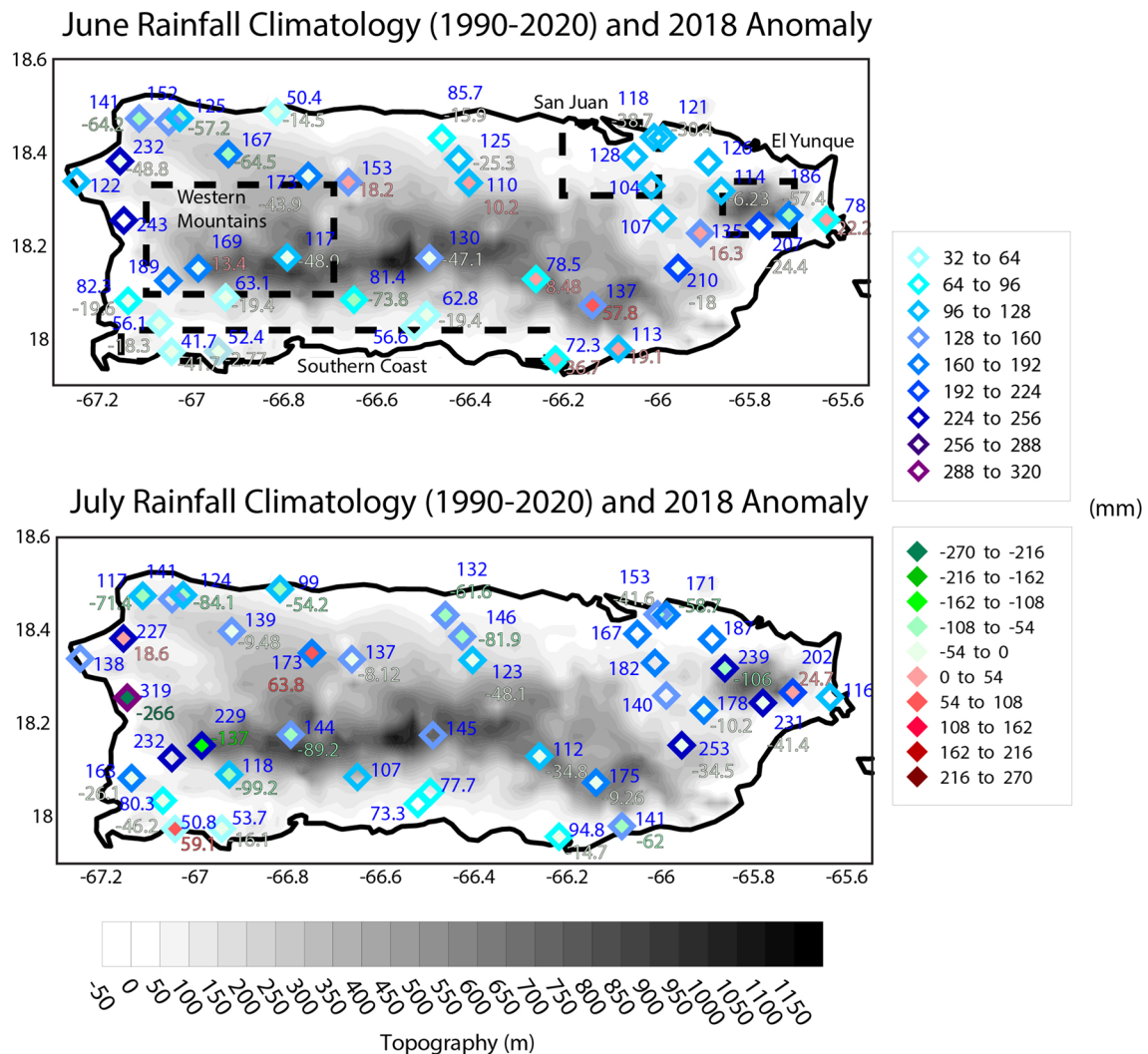
Figure 1. GHCN-based precipitation climatology (open diamonds and blue text) for June and July from 1990 to 2020, and departures from climatology (closed diamonds) for June and July 2018.

& González, 2011; Comarazamy et al., 2013; Hosannah et al., 2017; Jury et al., 2009). While the National Weather Service (NWS, 2016) indicates that ENSO also impacts the island's climate; approximately 13% more precipitation occurs during El Niño years in the dry season and 14% more precipitation occurs during La Niña years in the wet season, recent studies by Torres-Valcárcel (2018) and Hernández-Ayala (2019) found no significant correlation between ENSO and the island's rainfall despite the ENSO anomaly accounting for nearly 30% of rainfall variability over the Caribbean region. Generally, a warm ENSO (El Niño) event will result in negative sea surface temperature anomalies in the tropical North Atlantic and will lead to negative rainfall anomalies in the Caribbean region during the summer months. The opposite occurs for a cool ENSO (La Niña) event. According to NOAA's Oceanic Niño Index (ONI), the 2017–2018 period experienced weak La Niña conditions. The 3-month running ONI mean values for the dry season ranged between −0.9 and −0.7 and increased to −0.4 to 0.1 later in the year. Negative ONI values indicate a La Nina event and positive values indicate an El Niño event; values between −0.5 and −1 are considered weak La Niña periods and any value between −0.5 and 0.5 is considered ENSO neutral.

Charley et al. (2006) utilized over 50 years of rainfall and tropospheric pressure observations in the Caribbean region to establish that NAO is not correlated with rainfall totals in the Caribbean during periods of weakening La Niña. Since large-scale conditions were less convectively favorable for rainfall production in Puerto Rico during June and July 2018, rainfall in Puerto Rico the summer after Hurricane Maria was likely strongly influenced by local conditions. Hence the contributions of local convective processes to rainfall production cannot be ignored.

Local thermal (related to surface heating and sea breeze interaction) and mechanical (related to the orographic effect in which air is lifted over high elevations) convective processes have been shown to affect storm development in Puerto Rico (Hosannah et al., 2017; Jury et al., 2009; Laing, 2004), dominating storm production in the summer. Recent work by the authors has shown that 28% of convective storms occurring over Puerto Rico between June 2015 and June 2016 can be attributed to these local processes (Hosannah et al., 2019). The island's topography and land cover characteristics are integral to these interactions and assist in regulating spatiotemporal precipitation patterns. For example, elevated sites, such as Puerto Rico's Cordillera Central, the east-west oriented mountain range along the central axis (18.21°N), and the El Yunque natural rain forest on the eastern side of the island, induce orographic precipitation when they force moist air upwards (Jury, 2009). In addition, the easterly winds converge with westerly sea-breeze, inducing or intensifying afternoon convective storms. These two areas receive relatively high rainfall totals compared to the rest of the island. The orographic effect occurs at El Yunque as well as over the Cordillera Central. El Yunque is close to the east coast, and moist air is brought in by predominately easterly winds which fuel orographic precipitation at the site. The western portion of the Cordillera Central experiences the orographic effect in addition to sea breeze-easterly convergence, which does not occur to the same extent at El Yunque since the easterlies are the sea breeze in this case.

1.2. Hurricane Induced Land Cover Change

Boose et al. (1994) identified hurricane induced land damage to be the most influential factor impacting forest cover along the Gulf and Atlantic coasts. Ayala-Silva and Twumasi (2004) observed moderate Normalized Difference Vegetation Index (NDVI) changes across Puerto Rico after Hurricane Georges. These changes can persist for a decade or longer (Imbert & Portecop, 2008; Kok & Winograd, 2002), leading to drastic changes in the local climatology. Hurricane Katrina, a category 5 storm caused extensive forest damage over an 84,000 km^2 area in the Gulf coast (Chambers et al., 2007) and altered critical surface properties which modify surface-atmospheric interactions. These interactions govern local water and energy cycles and therefore impact convection and precipitation processes. Negrón-Juárez et al. (2008) observed that Hurricane Rita changed the albedo of 14,000 km^2 of forest along the Gulf, disturbing the climatological precipitation pattern for nearly 3 years; while the winter precipitation totals decreased, the summer totals increased.

Puerto Rico has diverse land cover; dry forests are located along the south-central coastal belt and the El Yunque (evergreen) forest is located on the slopes of the Luquillo Mountains in the north east (Kennaway & Helmer, 2007; Weaver & Murphy, 1990). Dry and moist serpentine forests are found in the north west. The

majority of the central to eastern locations are covered by moist forests—including the slopes of the Cordillera Central mountains. Grasslands are spread throughout the island at the base of the mountains (Helmer et al., 2002), with the largest pasture lands in the south west. In addition to the San Juan Metropolitan Area, developed land includes Mayaguez in the west, Caguas in the east and Ponce in the south, each with populations of over 100,000. Cultivated land (sugarcane, fruits, and vegetables) is also found across the southern part of the island. Undeveloped and unirrigated barren land cover is mostly distributed in the southwestern and south-central parts of the island. Lastly, wetlands account for a minute portion of the island.

Hurricane Maria caused extensive damage by uprooting trees and causing wide-spread flooding—conditions which have been shown to modify the radiation balance, reduce the moisture capacity of vegetation, and influence the partitioning of surface energy fluxes (Negrón-Juárez et al., 2008). Maria also severely defoliated forest canopy and deposited massive amounts of litterfall across the island. Liu et al. (2018) investigated litterfall in four of Puerto Rico's forests (Guánica State Forest, Río Abajo State Forest, Guayama Research Area, and Luquillo Experiment Forest) before and after Hurricanes Irma and Maria and calculated a litterfall deposit ranging from 95% to 171% of the average annual litterfall production, with leaffall and woodfall amounting to 63%–88% and 122%–763% of the annual totals, respectively. Feng et al. (2018) used Landsat 8 image composites to compare pre and postMaria land characteristics and reported severe damage to 23–31 million trees. Work by Jury et al. (2019) showed a reduction in vegetation over Puerto Rico—indicated by NDVI decreases across the island. Hu and Smith (2018) also reported a drop in NDVI after Hurricane Maria's landfall (decreased by approximately 0.2), returning to near normal vegetation after 1.5 months.

Miller et al. (2019b) showed that Hurricane Maria damage impacted daily cloud activity, indicating that postMaria land-atmosphere interactions were modified during the dry season. Although Miller et al. (2019a) did not conclusively attribute hydrological changes to Maria's defoliation, they note that the changes were consistent with the theoretical implications of a major hurricane. Hence, land cover modification from Hurricane Maria may lead to profound impacts on the island's rainfall climatology. Therefore, postMaria Puerto Rico was a rare opportunity to monitor land cover changes and the associated land-atmosphere interactions, contributing to the understanding of local convective processes in the tropical environment. With the intensity of hurricanes expected to increase in the coming years (Bender et al., 2010; T. Knutson et al., 2020), improved understanding of how land change may impact the climate is necessary. The current study therefore seeks to answer the following questions:

- How has Hurricane Maria impacted the land cover/land use distribution in Puerto Rico?
- How has the surface energy budget changed across the island?
- What are the implications for convection and precipitation processes?

To answer these questions, we pair the occurrence of the RAPID-CAST field campaign with numerical experiments conducted via the Regional Atmospheric Modeling System (RAMS). The following sections detail the methods used to quantify the changes in land cover characteristics and the numerical experiments to investigate the impact of these modifications to island-wide surface-atmospheric interactions and precipitation.

2. Methodology

2.1. RAPID-CAST

During the RAPID-CAST campaign (June 24 to July 3, 2018), surface-atmospheric variables were continuously monitored via a comprehensive energy balance site installed at Finca Alzamora (18.22°N, 67.15°W), on the University of Puerto Rico Mayaguez (UPRM) campus. The site included a flux tower with a 3-D sonic anemometer, a virtual temperature and humidity sensor, an infrared gas analyzer, a rain gauge, a four-component radiometer, and a pressure sensor. Ground sensors include heat flux and soil moisture sensors. The site allows for the characterization of surface driven processes. Radiosondes were also launched at UPRM to determine local instability (mixed layer convective available potential energy (MLCAPE) and lifted index (LI)), available water, and the vertical structure in the lower troposphere. Due to NWS forecasts suggesting

minimal rainfall and permissions granted by the San Juan International Airport, UPRM launches occurred from 26 to June 30, 2018.

2.2. Satellite Imagery

The land cover analysis involved implementation of satellite derived images to quantify the Hurricane Maria induced land cover change. Two satellite image mosaics were created using LANDSAT 8 OLI/TIRS C1 Level-1 multispectral images (30 m resolution). The images employed were within one year before (pre) and after (post) Maria to ensure that the mosaics represent the island's land cover close to the hurricane. Images from October 16, 2016 to June 22, 2017 were collected for the preMaria mosaic and images from October 3, 2017 to June 25, 2018 were collected for the postMaria mosaic. Clouds and cloud shadows were detected and removed using the Fmask 4.0 algorithm (Zhu et al., 2015). The resulting products were cloudless images encompassing only the main island, which were then superimposed to create the mosaics. This method ensures masked empty spaces in one image were filled up with data from the subsequent image (Figure S1a). To guarantee that the mosaics were weighted toward pre and postMaria conditions, dates closer to Hurricane Maria took precedence over other dates in the mosaics. To create the preMaria mosaic the image from June 22, 2017 was prioritized followed by the next closest date until October 16, 2016. This was reversed to create the postMaria mosaic wherein the image from October 3, 2017 (the closest image postMaria) was prioritized followed by later dates. Figure S1b indicates the order of the image dates in each mosaic and their relation to the date of the hurricane.

A seven-type land cover classification was performed on each mosaic. The classes, including developed, water, wetlands, cultivated, barren, herbaceous, and forest land types, were modeled from the 2001 MultiResolution Land Cover Characteristics (MRLC) Consortium's National Land Cover Database (NLCD, Homer et al. 2004) product. The pre and postMaria land classes were then transformed on a per 1 km resolution pixel basis for implementation in the RAMS (Cotton et al., 2003; Pielke et al., 1992) version 6.2.06 numerical cloud resolving model (described in Section 2.3). An NDVI analysis was also conducted using LANDSAT-8 bands 4 (visible red) and 5 (near infrared).

2.3. RAMS Simulations

The RAMS domain included the North Tropical Atlantic and Caribbean Sea 75°W-58°W and 10°N-26°N at the coarse grid (30 km resolution), and two finer grids covering 68°W-64.5°W and 17°N-19.5°N (5 km) and 67.45°W-65.55°W and 17.85°N-18.6°N (1 km) covered the main island of Puerto Rico. Each simulation had 41 vertical levels, a long time-step of 30 s, and a short time step of 5 s. The two landclass mosaics described in Section 2.2 were assimilated into the land ecosystem-atmosphere feedback (LEAF-3) sub model of RAMS for grid 3. LEAF-3 evaluates energy and water budgets at the surface, and therefore simulations with modified land surface configurations allow for estimation of land change impacts on convection and rainfall production. The Harrington (1997) scheme was implemented for short and longwave radiation as it accounts for cloud water, rain, aggregates, graupel, hail, water vapor, and ice crystals. For grid 3, an explicit cloud microphysics scheme (Saleeby & van den Heever, 2013) is used. The Kuo convective scheme was used on grid 1 (Molinari, 1985; Tremback, 1990).

The two simulations were focused on the period encompassing June 23, 2018 to July 2, 2018—covering the RAPID-CAST campaign. The simulations were driven by final data (FNL) at 1° by 1° spatial resolution from the National Center for Environmental Prediction (NCEP), updated every 6 h (National Centers for Environmental Prediction/National Weather Service/NOAA/U.S. Department of Commerce, 2000). FNL analyses include surface pressure, sea level pressure, geopotential height, soil and air temperature, sea surface temperature, soil water content, relative humidity, u and v winds, and vertical motion from the surface up to 10 millibars. Prognostic variables of interest within RAMS include surface temperature, liquid water content, short and longwave radiation, sensible and latent fluxes, precipitation, wind speed and direction, and humidity. AHPS precipitation data was compared to both cases. As both the pre and postMaria land cover simulations were conducted with the same FNL data, the simulations reflect a comparison between
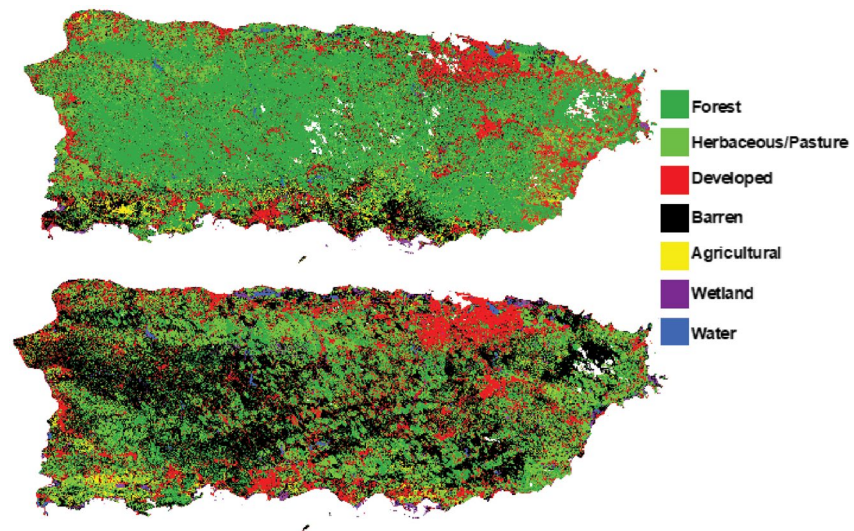
Figure 2. Pre and post land cover.

the damaged condition (postMaria land cover) and the case wherein the land cover was unaltered (preMaria land cover).

3. Results

3.1. NDVI and Land Cover Changes

The NDVI analysis (LANDSAT-8, Figure S2) indicates decreased NDVI across the island after Hurricane Maria—particularly over El Yunque (peaks ranging from 0.75 pre to 0.55 postMaria), along the north coast (from 0.8 to 0.5), and at the center (from 0.9 to 0.7) of the island while NDVI increases are found in the south (0.55–0.75).

Despite efforts to create full island LANDSAT-8 image mosaics, small patches (indicated by white pixels) without data over the Cordillera Central and El Yunque areas remain. Figure 2 (top panel) shows the land cover characteristics of preMaria Puerto Rico. Fifty-three percent of the land cover was forest, with dry forests located along the south-central coast, largely virgin evergreen forests within El Yunque at the eastern side of the island, dry/moist serpentine forests in the north west and mostly moist forests in the central to eastern areas. The grasslands accounted for 16% of the island, and developed land accounted for 14%. Approximately 4% of the island was cultivated land—the majority of which is found in the south. Approximately 1% of the island was wetlands, and the remaining 13% was identified as barren land. Figure 2 and Table 1 detail the land cover characteristics for pre and postMaria states. One of the most visible features postMaria is the increase of barren and pasture land cover throughout the island. Most of the forest cover island-wide apart from the south has been severely impacted, with the satellite imagery indicating a decrease from 53% preMaria to 11% postMaria. The northwest exhibits the most forest damage followed by the central region and El Yunque. The grass cover also increased from 15.45% to 26.30%. The cultivated land cover has decreased by 0.76% and the wetlands and water have increased marginally.

An aerial drone survey was conducted in Mayaguez from March to November of 2018 to track recovery over an area heavily damaged by Hurricane Maria (Figure S3). The area (0.35–0.65 km^2), heavily populated by trees and grass, suffered severe defoliation and tree damage. Although the area had recovered slightly by March 2018, it was not fully green until August 2018. Even then, some of the damaged trees were replaced by grass. These results are the basis for our idealized transformation of the severely damaged trees to barren land and pasture.
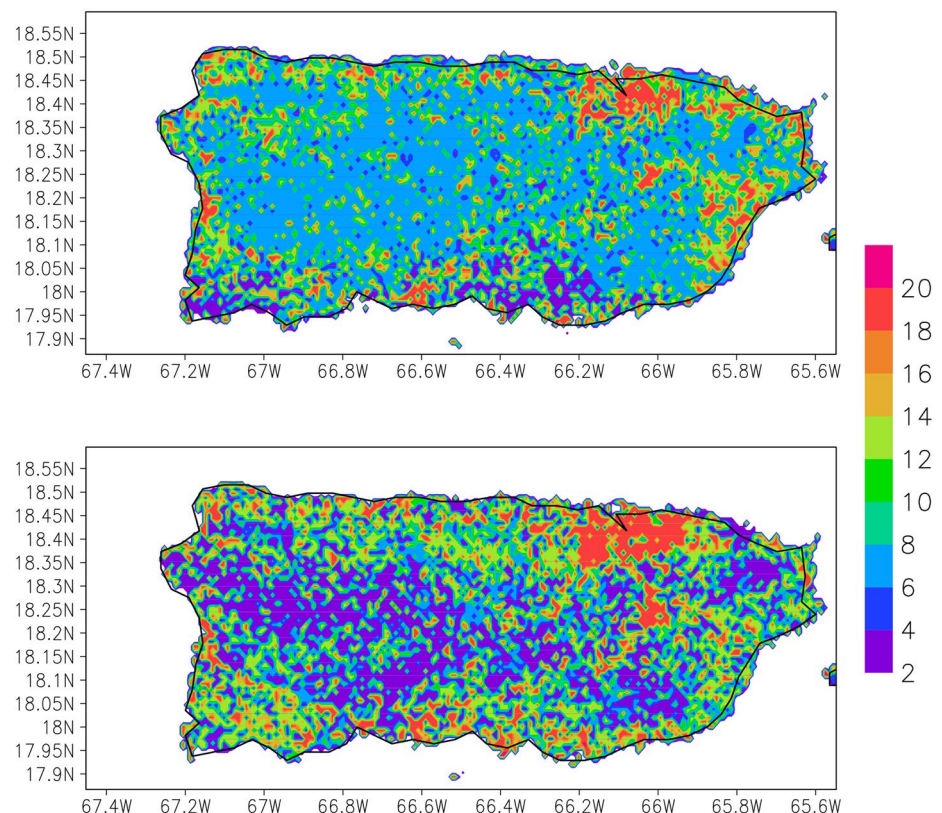
Table 1
Pre and PostMaria Land Cover Class Distribution

	Developed	Water	Wetlands	Agricultural	Barren	Herbaceous	Forest
PreMaria	13.86%	0.31%	0.99%	3.53%	12.92%	15.45%	52.94%
PostMaria	16.93%	0.56%	1.61%	2.77%	41.27%	26.30%	10.56%

3.2. Impact on Surface Energy Budget

The pre and postMaria landclass mosaics were transformed on a per 1 km resolution pixel basis for implementation in the LEAF-3 sub model of the RAMS numerical cloud resolving model (described in Section 2.3). Figure 3 shows the final model assimilated 1 km pre and postMaria domains. The initialization properties of all associated LEAF-3 land classes are listed in Table 2.

Results for longwave and shortwave up radiation, sensible and latent heat fluxes, and liquid buoyancy (10-day averages) from 12:00 to 16:00 AST are presented henceforth as this range covers the most convectively active period during summer days, when intense local storms are most prevalent. Downwelling long and shortwave radiation are not shown since both simulations were forced by identical data. Upwelling long-wave radiation values steadily increased from 12:00 to 14:00 AST and decreased from 14:00 to 16:00 AST in both cases (Figure 4). As values are predominantly influenced by land cover emissivity, noticeable changes are observed across the island as a result of the forest to bare soil/grass conversion. The average values have mainly increased in the postMaria case by 25 W m^{-2} across the island, with some areas in the center of the island where the preMaria case exhibits higher values by 25–30 W m^{-2}. Similar increases in upwelling short-wave radiation, which is dependent on albedo, are noted for the postMaria case (Figure 5). Shortwave values steadily increased from 12:00 to 14:00 AST and decreased from 14:00 to 16:00 AST in both simulations. The


Figure 3. PreMaria (top) and postMaria (bottom) land cover for grid 3.

Table 2
Properties of LEAF-3 Land Classes

Land cover type	Class number	Albedo (green)	Albedo (brown)	Emissivity	Solar radiation	Tai (max)	Veg ht	Veg frac
Water	1	0	0	0	0	0	0	0
Bare soil	3	0	0	0	0	0	0	0
Forest	5,6	0.14	0.24	0.95	8.0	8.0	22.0	0.8
Short grass	8	0.21	0.43	0.96	5.1	4.0	0.3	0.75
Agricultural	15	0.22	0.40	0.95	5.1	5.0	1.0	0.85
Wetland	20	0.17	0.24	0.95	4.1	7.0	32.0	0.90
Urban	19	0.20	0.36	0.90	5.1	3.6	6.0	0.74
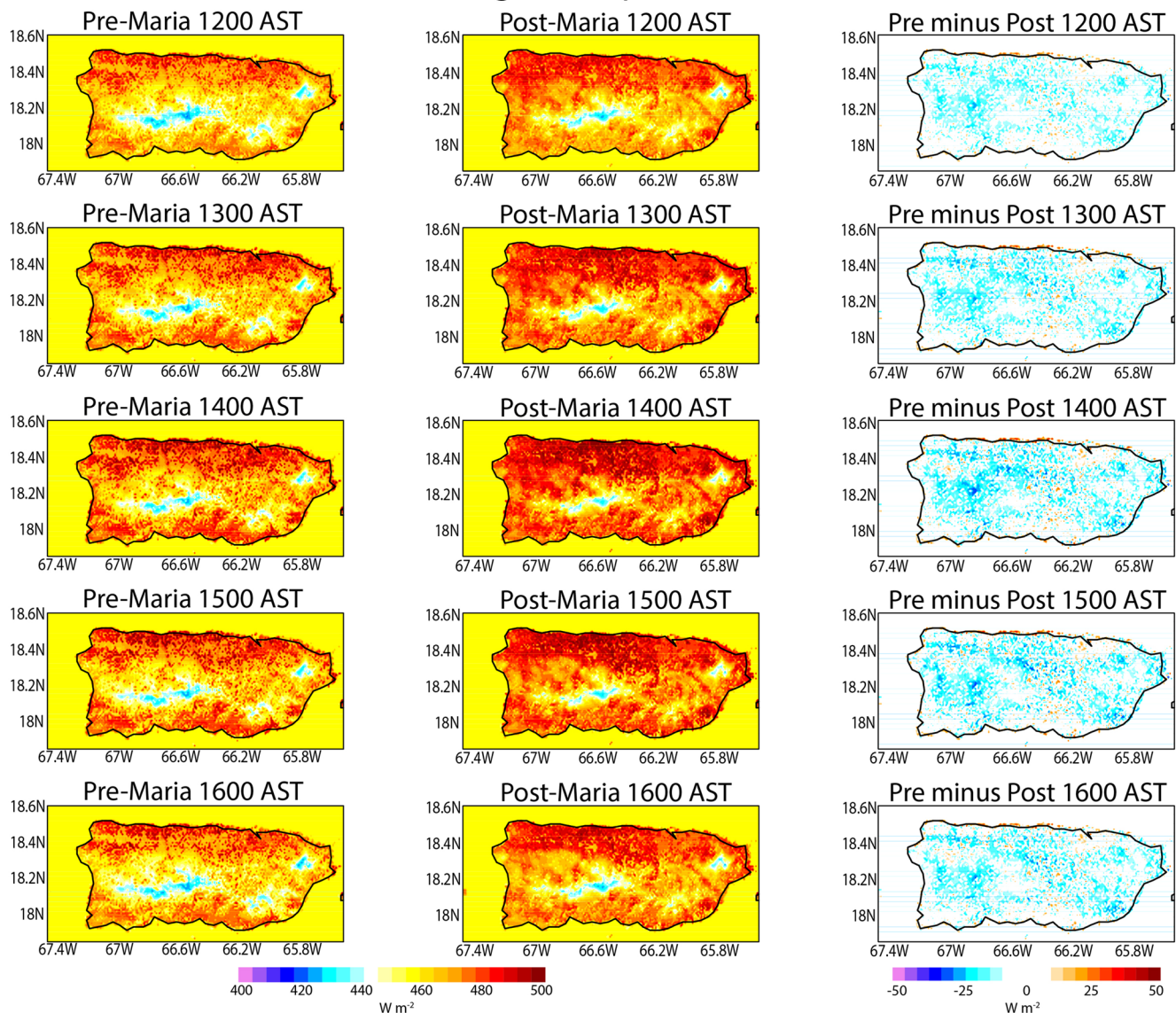
Figure 4. Island-wide upwelling longwave radiation for pre and post land cover from 12:00 to 16:00 AST.
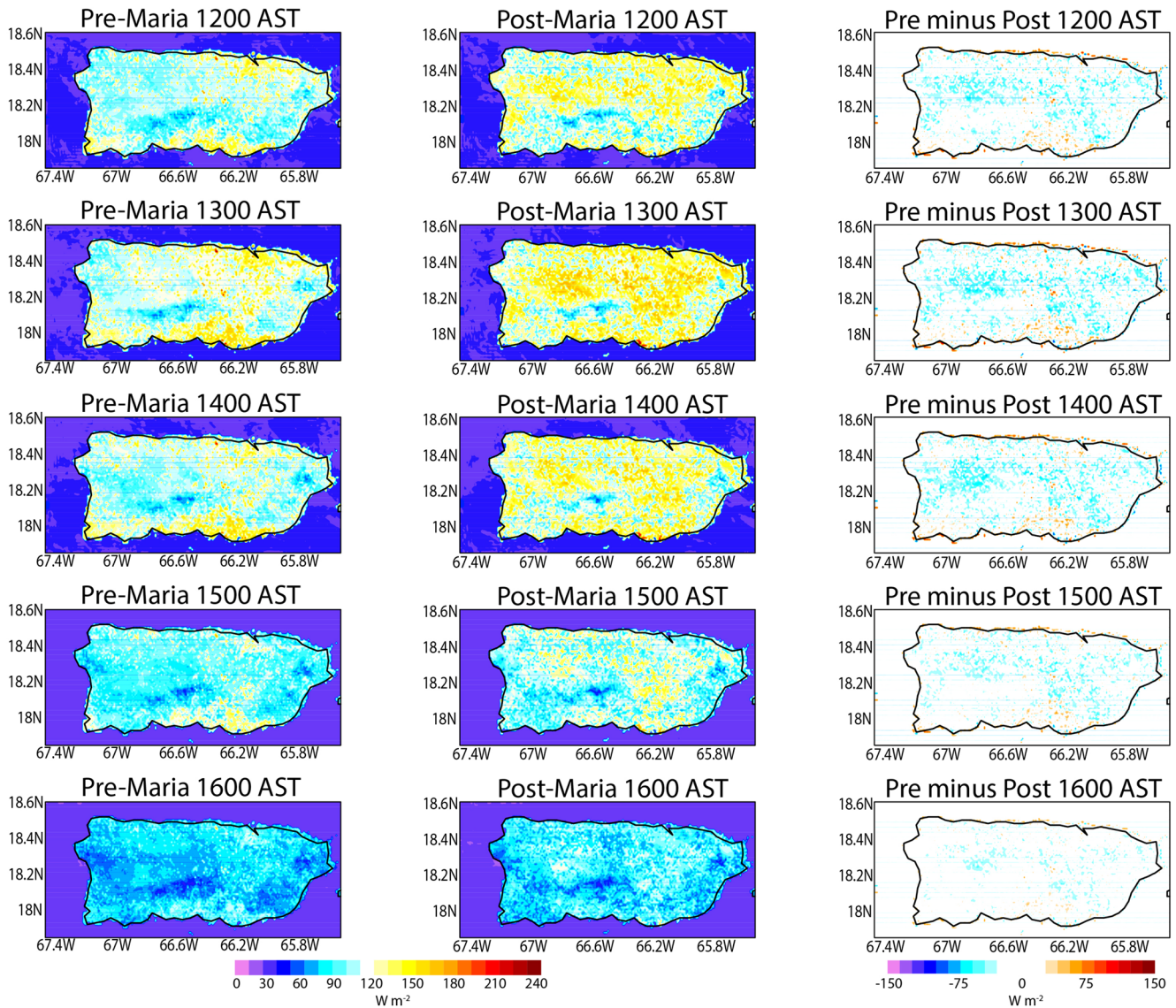
Figure 5. Island-wide upwelling shortwave radiation for pre and post land cover from 12:00 to 16:00 AST.

largest changes between pre and postMaria conditions occur across the central and northern areas with averages ranging from 60 to 200 W m^{-2}.

Sensible heat flux (Figure 6) decreased sharply across the island as a result of the land cover changes, with the center to the west (66.5°W-67.15°W) and northeast of El Yunque (65.7°W, 18.38°N) showing the largest changes (up to 150 Wm^{-2} higher in the preMaria scenario) between cases. Along the north coast (75 Wm^{-2}) and in the east, the preMaria case exhibits values 75–100 Wm^{-2} higher than the postMaria case. Values increased from 12:00 to 14:00 AST and decreased from 14:00 to 16:00 AST in both simulations. Maximum sensible heat fluxes in the north (except the SJMR) decreased substantially between pre and postcases by 75–100 Wm^{-2}. Sensible heat flux in the southeastern and southwestern coastal regions increased in the postcase by 75 Wm^{-2} while values on the southern coast bounded by 66.9°W and 66.2°W indicate decreases of approximately 50 Wm^{-2}. There are smaller changes between pre and postMaria land cover conditions in the late afternoon.

Latent heat fluxes for both cases (Figure 7) show similar spatial patterns despite significantly higher values in the postMaria case. Values increase from 12:00 to 14:00 AST and decrease from 14:00 to 16:00 AST in both
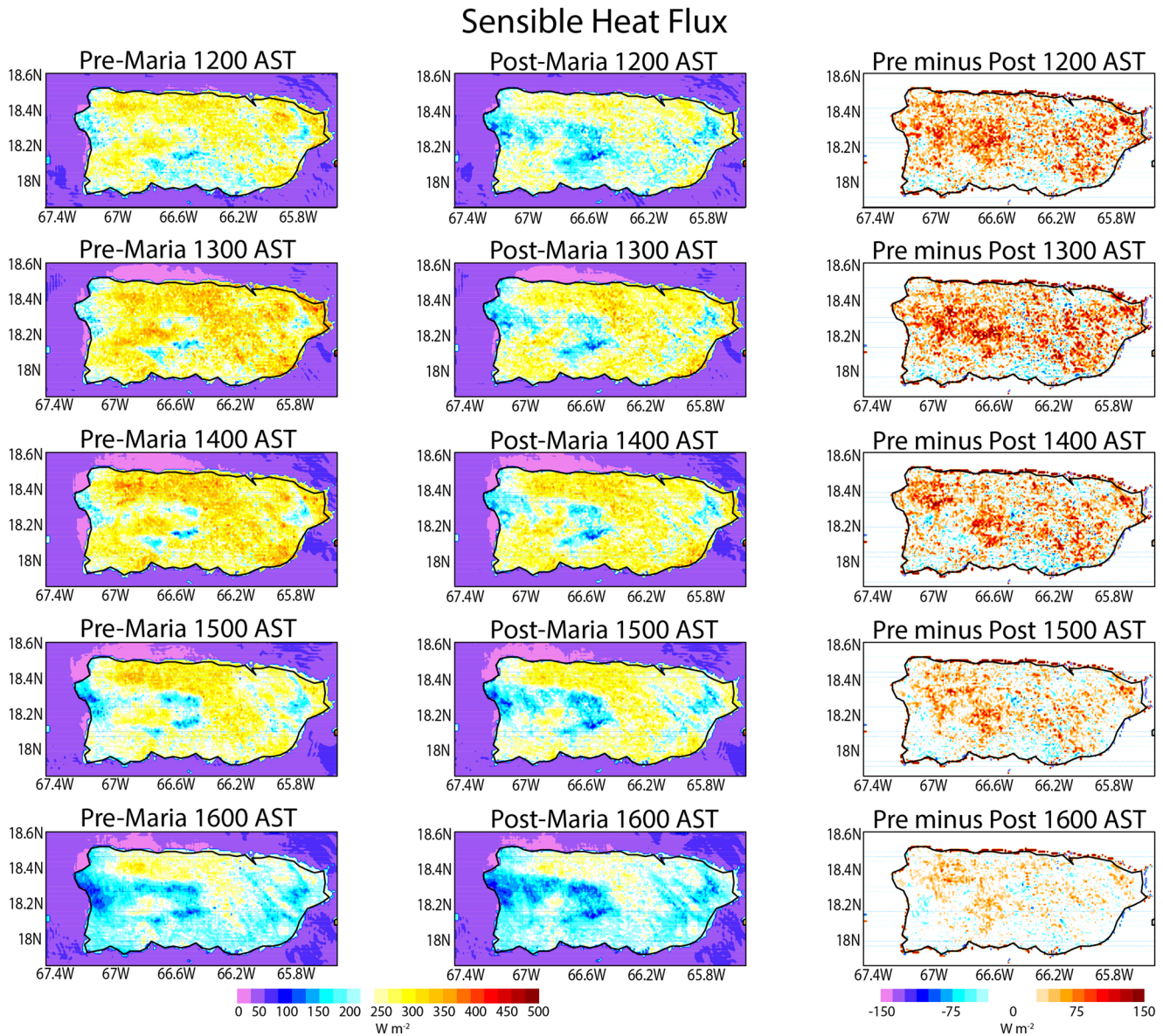
Figure 6. Sensible heat flux from pre and postMaria land cover from 12:00 to 16:00 AST.

cases. The postMaria simulation exhibits latent heat flux surpluses over El Yunque and in the northwest quadrant of up to 150 Wm^{-2}. Along the northern coast, the values differ marginally—100 Wm^{-2} (pre) and 125 Wm^{-2} (post). There are also locations at the center of the island and at the west coast where preconditions produce latent heat fluxes 125 Wm^{-2} higher than postvalues. Unlike the sensible heat flux, there are significant differences in latent heat between pre and postMaria scenarios during the late afternoon periods.

3.3. Impact on Boundary-Layer Characteristics

As with all previously investigated variables, liquid water buoyancy, the rate of change of the vertical velocity of liquid in air (Figure 8) increases from 12:00 to 14:00 AST and decreases from 14:00 to 16:00 AST in both simulations, with increased values over the northwest and El Yunque in the preMaria case (0.05 m s^{-1}). However, by 14:00 AST, the postMaria case produces higher buoyancy (up to 0.04 m s^{-1}) between 67°W and 66.7°W and 18.2°N and 18.4°N, as well as 66.5°W to 66.3°W and 18.2°N and 18.4°N.
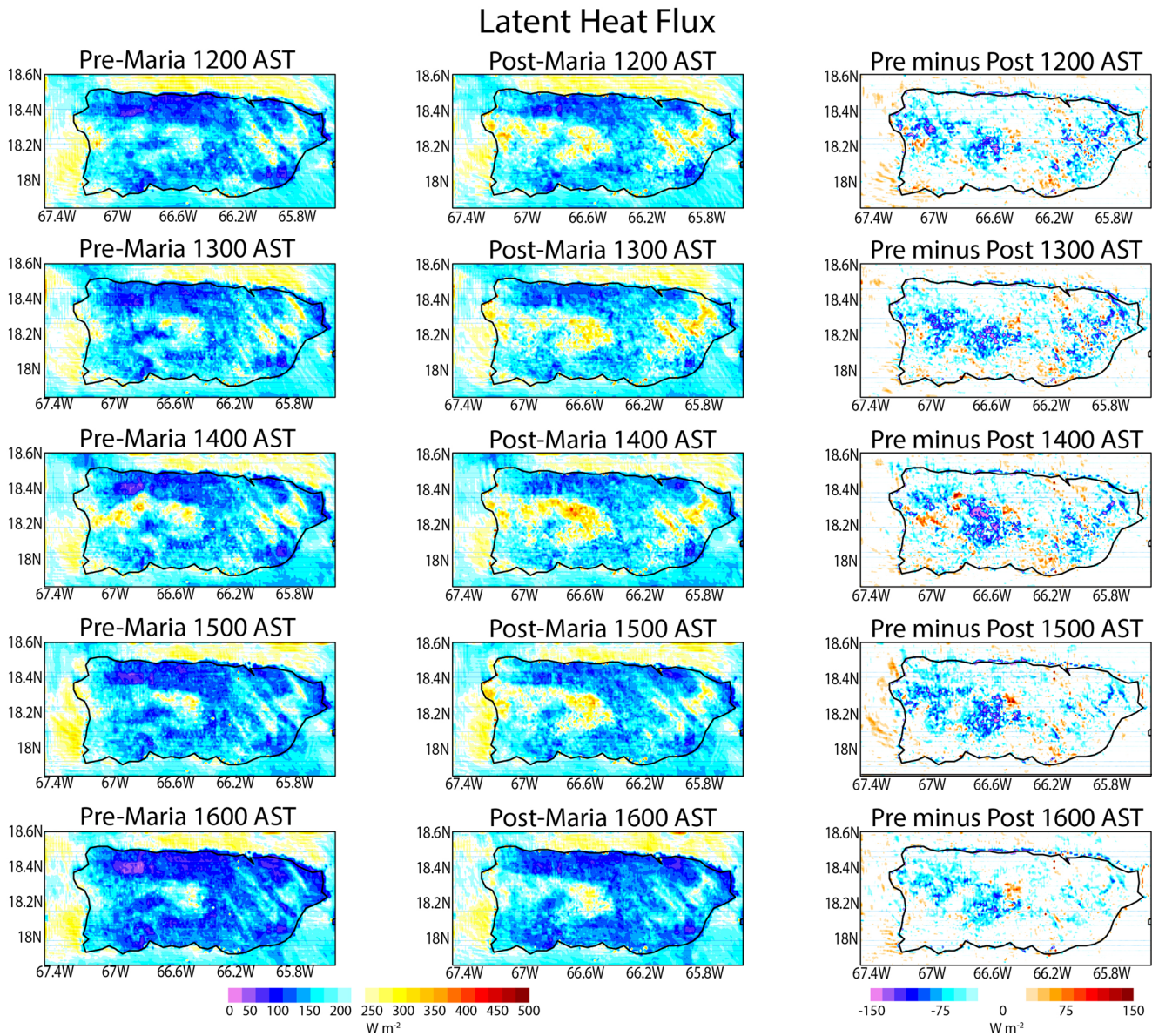
Figure 7. Latent heat flux for pre and postMaria land cover from 12:00 to 16:00 AST.

The evaporative fraction (EF) is the ratio of latent heat flux to available energy. Values during 09:00-16:00 AST (the nighttime EF drops to zero) at SJMA and three of the most affected areas (El Yunque, the Western Mountains, and the Southern Coast) from June 23 to July 2, 2018 (Figure 9) reveal notable differences between the pre and postMaria cases. The EF at El Yunque in the postMaria case exceeds preMaria values by up to 200% (June 24–27, 2018). The difference is less pronounced at the Western Mountains, although still considerable (50% more in the preMaria case). At San Juan and the Southern Coast, the values between both simulations are similar.

Figure 10 shows changes in convection mostly over the Western Mountains and El Yunque. Positive values are related to air ascension; negative values represent descending air. At both the western portion of El Yunque and the Cordillera Central mountains, the peak updrafts and downdrafts are stronger in the postMaria scenario. The peak updrafts are 0.09 and 0.095 ms^{-1} respectively (June 28–29, 2018) while peak downdrafts postMaria are −0.06 and −0.09 ms^{-1} respectively (June 24–26, 2018), coinciding with the maximum EF differences between pre and postMaria cases (Figure 9). It should also be noted that the convection differences
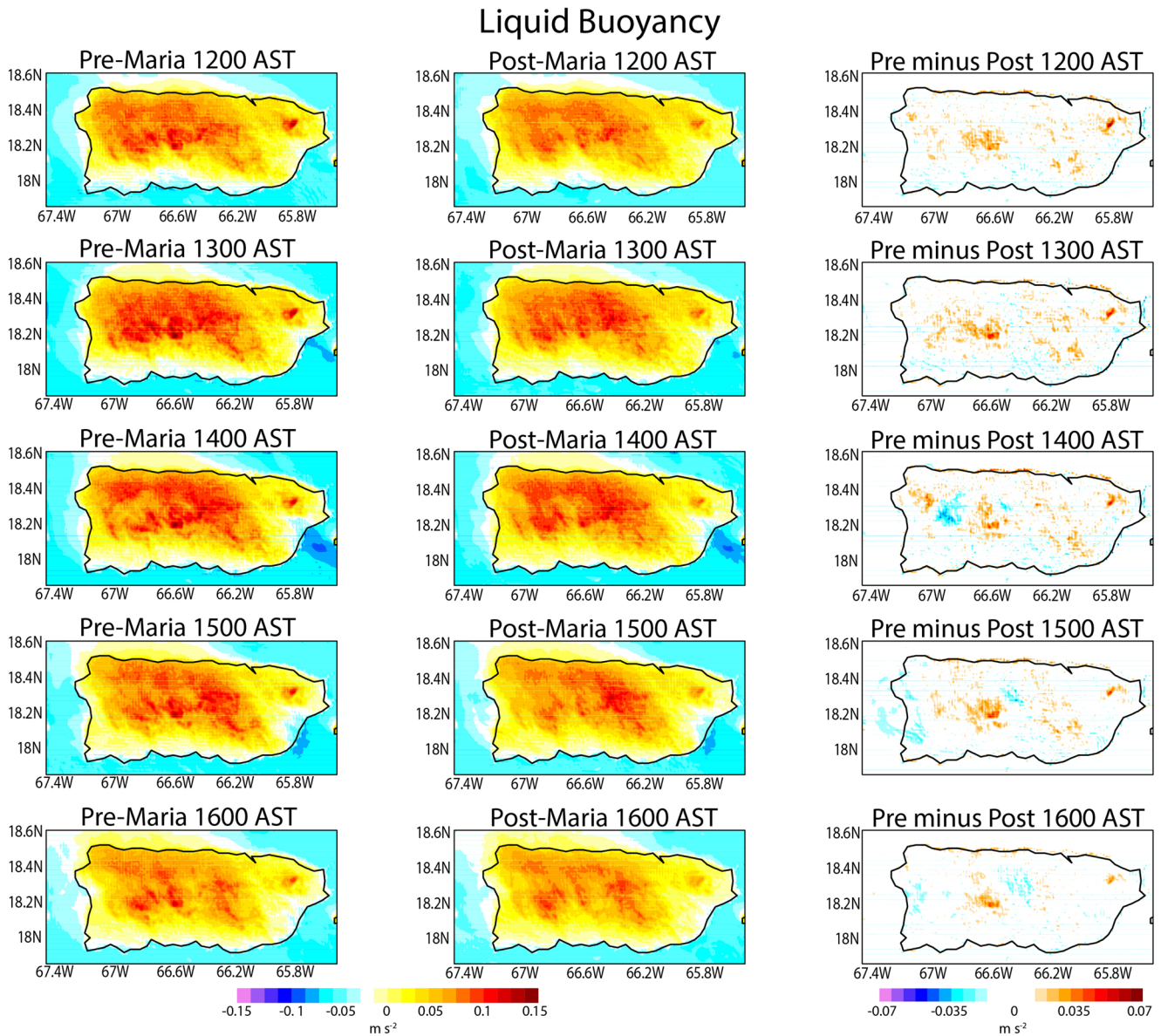
Figure 8. Buoyancy of liquid for pre and postMaria land cover from 12:00 to 16:00 AST.

between the two scenarios are negligible over San Juan and the Southern Coast. This leads to the possibility that changes in the horizontal wind over the study period (convergence modification) may have led to changes in convection over El Yunque and the Western Mountains.

3.4. Possible Impact on Local Precipitation

MLCAPE, LI, and available precipitable water were calculated using radiosonde launches at TJSJ (east) and at UPRM (west) to ascertain the local convective conditions during RAPID-CAST (Table 3). The eastern launches occurred at 08:00 and 20:00 AST daily. The launches on the west occurred between the hours of 11:00 and 17:30 AST (the UPRM launch on June 30, 2018 lost signal after launch). The 4-day radiosonde comparison indicates varied conditions at the two locations although the western radiosondes did not reach as high as the eastern ones. For comparison purposes, the MLCAPE was calculated from 0 to 8 km. Although a small sample, higher values of precipitable water, and more unstable LI values are found on the
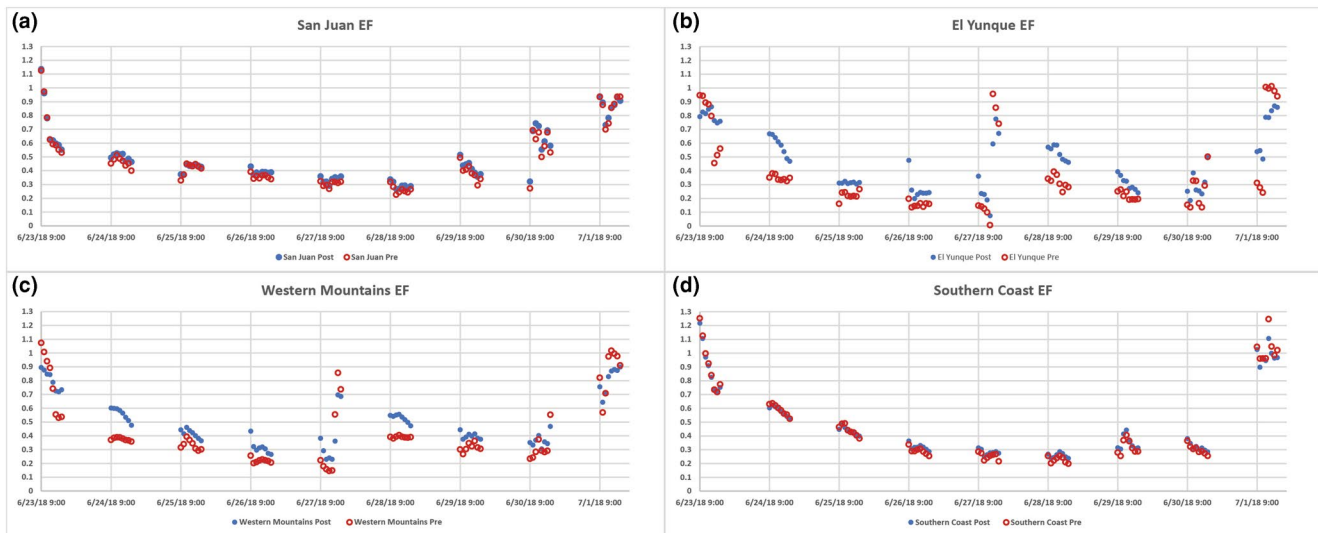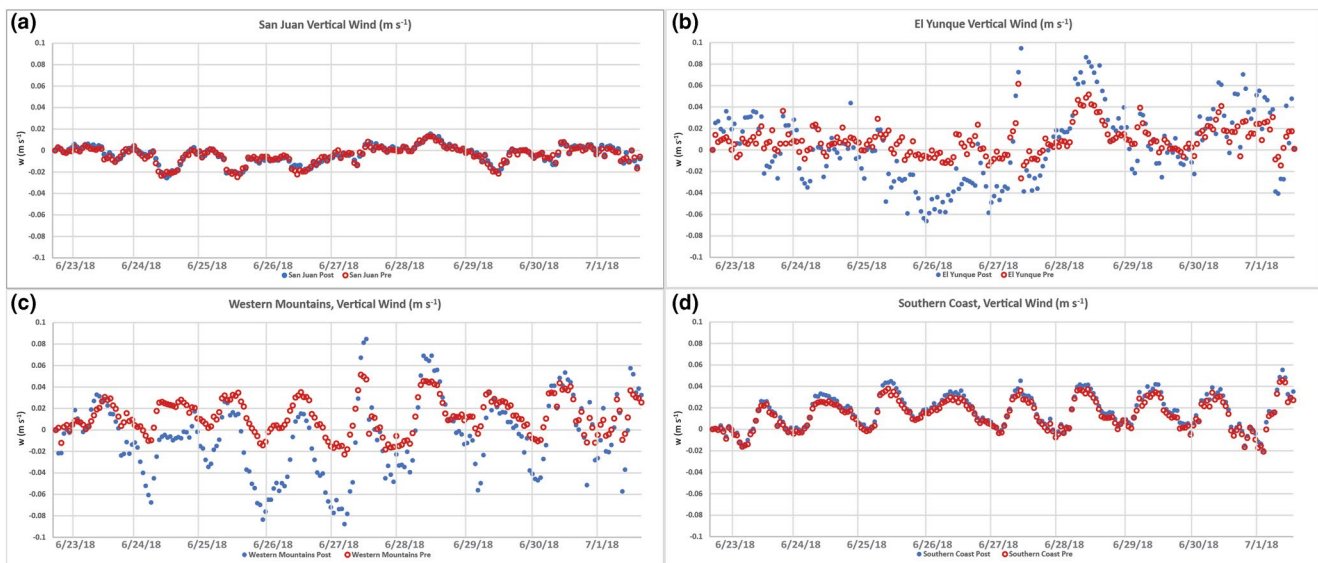
Figure 9. The evaporative fraction for pre (open, red) and post (solid, blue) simulations at the (a) San Juan, (b) El Yunque, (c) Western Mountains, and the (d) Southern Coast areas.

west. There is evidence of westerly sea-breeze in the lower 1.5 km for all western launches, whereas the wind direction in the lower 2 km for the eastern launches range from southeasterly to easterly.

The June 28, 2018 rainfall event was selected for further study of how land modification may impact local storm development because the rainfall occurred over areas with severe Hurricane Maria induced damage (Figure 11d). The storm produced moderate rainfall to the left of the diagonal extending from the northeast to the southwest corners of the island (black dashed line). The rain was produced as high pressure maintained north of the island, and moderate easterly winds flowed at the surface—laden with Saharan dust traveling west ahead of a tropical wave. Radiosondes launched during June 28, 2019 at 12:54 and 17:03 AST at Mayaguez indicate a change from a dry environment in the early afternoon to a moist environment by the late afternoon. Between the surface and 2 km, the 12:54 AST data indicates an increase in relative humidity

Figure 10. The vertical wind (w) for pre (open, red) and post (solid, blue) simulations at the (a) San Juan, (b) El Yunque, (c) Western Mountains, and the (d) Southern Coast areas.

Table 3
RAPID-CAST Radiosonde Data

Date	MLCAPE (J kg^{-1}) (TJSJ)	MLCAPE (J kg^{-1}) (UPRM)	LI (TJSJ)	LI (UPRM)	Water (mm) (TJSJ)	Water (mm) (UPRM)
26 June	638,443	499	−3.1, −1.9	−3.3	41, 40	47
27 June	579,708	848	−3.3, −5.1	−5	40, 40	46
28 June	280,530	132,579	−1.9, −2.4	−1.9, −3.4	37, 41	46, 50
29 June	86,867	86,264,473	−0.7, −5.6	−0.1, −2.5, −3.6	40, 44	42, 43, 46
30 June	540,684	------	−1.4, −3.7	------	40, 35	------

Note. Launches on the same day are separated by commas.

from 55% to 95%. Above 2 km, the humidity decreased from 95% to 30% by 6 km. The 17:03 AST data indicates relative humidity at the surface exceeding 85%, increasing to 95% by 1.5 km, constant until 3.5 km. Above 3.5 km, the humidity decreased to 65% by 5.5 km. The radiosondes also indicate early afternoon westerly sea-breeze between the surface and 1 km.

Figures 11a and 11b show the total accumulated precipitation for post and preMaria simulations, respectively. The model produces higher rainfall totals (70 mm) than the AHPS product indicates (55 mm) along the central latitude of the island (18.21°N) and shows a slight deviation from the AHPS totals as shown in Figure 11d. Despite shifting the observed San Juan precipitation southward, the model captures the general orientation of the event in both pre and postMaria land cover simulations, producing the highest totals
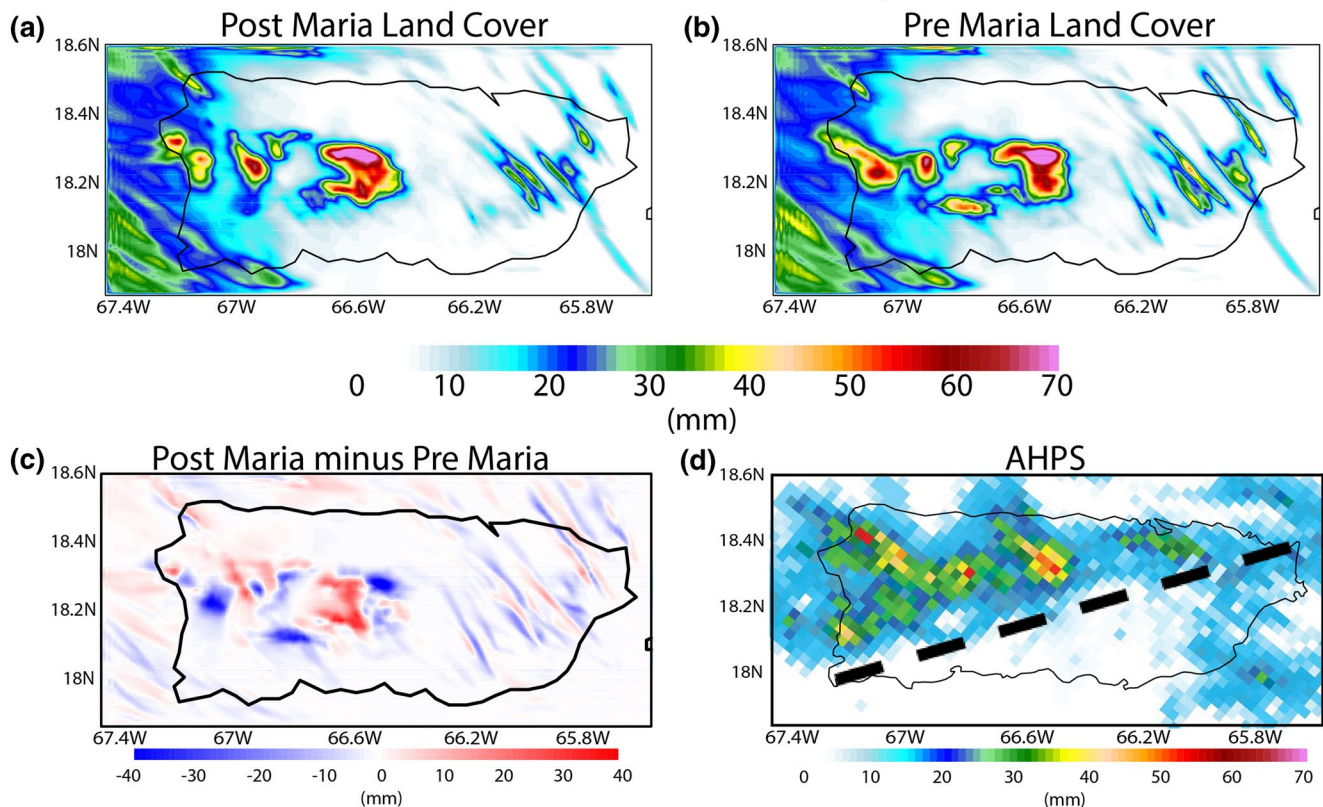
Figure 11. Total accumulated precipitation for (a) postMaria land cover, (b) preMaria land cover, (c) postpre difference, and (d) RAPID-CAST storm event from the Advanced Hydrological Prediction Service (AHPS) on June 28, 2018.

28 June 2018 u v Winds
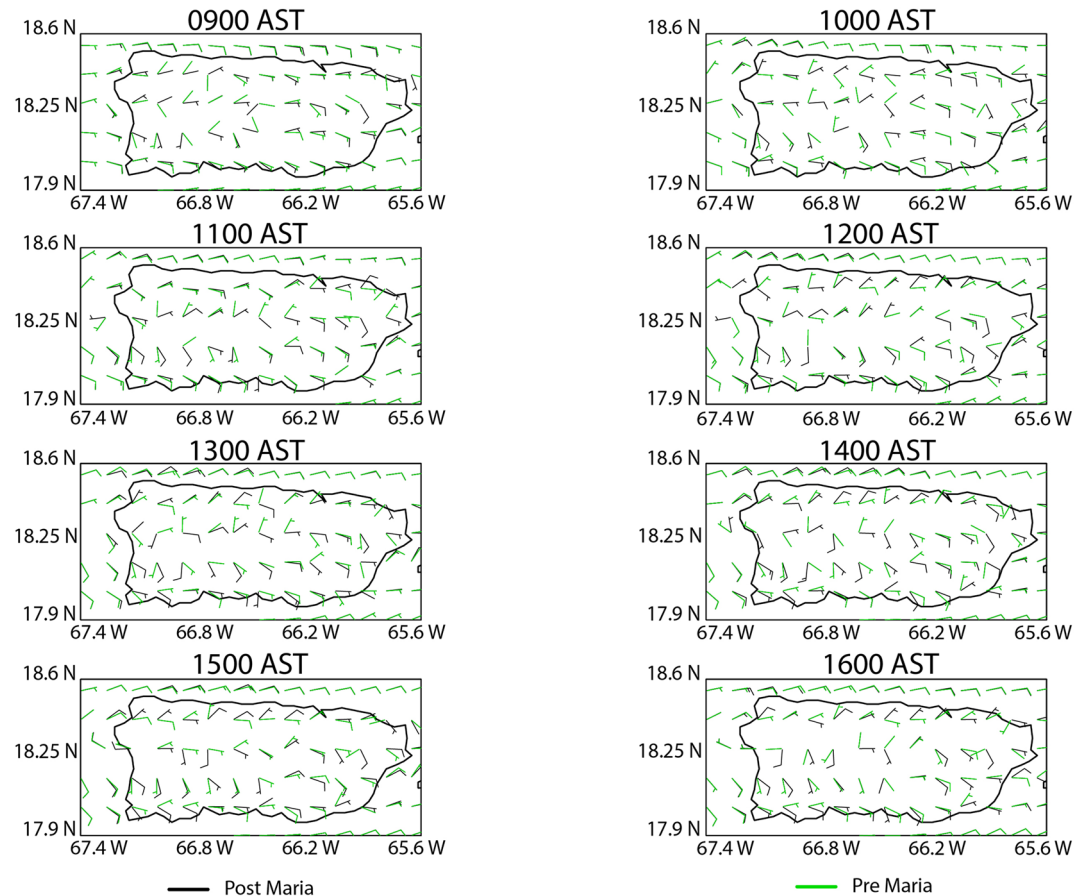
Figure 12. Wind differences between pre (green) and post (black) Maria wind speed and direction on June 28, 2018 from 09:00 to 16:00 AST.

over similar locations as in the observations. An additional precipitation cell centered at 66.8°W, 18.15°N is present in the preMaria case. A difference plot of the postminus preMaria totals (Figure 11c) shows the highest deviations between the two cases over the western mountains (67.15°W-66.4°W, between 18.1°N and 18.3°N), although a clear pattern is not evident as these results reveal a "+−+−" pattern.

Lower precipitation modifications (10–20 mm) are also shown over the eastern side of the island within proximity of El Yunque (65.8°W, 18.25°N). Latent heat during the 12:00–16:00 AST period of June 28, 2018 is highest across the west-central portion of the Cordillera Central mountain range (Figure S4), with values in the postMaria case exceeding the preMaria case by 400 Wm^{-2} over most of the west-central region, although there exist smaller pockets at the west coast, at the center of the island, and at 18.15°N exist where the preMaria values exceed the postMaria values by 350 Wm^{-2}. The sensible heat (Figure S5) is highest across the northern coast and the east-central portion of the island, with values in the preMaria case exceeding the postMaria case by 350 Wm^{-2} over most of the west-central region, although a "+−+−" pattern is identifiable across every portion except the central western area. These sensible and latent heat findings are in agreement with the 10-day averages (Figures 6 and 7). Lastly, the southern coast which experienced minimal convection changes, indicates no difference in precipitation between pre and postMaria cases, supporting the sensible/latent heat, buoyancy (Figure 8), EF (Figure 9), and vertical wind (Figure 10) results.

The hourly surface u v wind evolution from 09:00 to 16:00 AST for each case are plotted in Figure 12. From as early as 11:00 AST, the westerly sea breeze is present on the west coast in the postMaria case, and appears to orient westerly around 14:00 AST in preMaria case.

4. Discussion

As evidenced by NDVI and the land cover change analysis, Puerto Rico suffered significant damage to its land cover (excluding the south). Approximately 80% of the forest cover was affected. Northwestern Puerto Rico exhibited the most forest damage followed by the central region and El Yunque; much of the forest change registers as pasture and barren land cover. Cultivated land decreased while the wetlands and water types increased marginally. In the context of Feng et al. (2018) and Liu et al. (2018), these results suggest that the barren land cover consisted of large quantities of tree woodfall and leaffall. The increase in wetlands is possibly a result of overly saturated terrain caused by heavy rainfall. The increase in developed land cover in the SJMA could be related to improved visibility from the satellite to the surface due to reduced foliage and trees.

Across the island, the interactions between the local scale processes and the large-scale systems contribute to precipitation patterns and intensity. Modern-Era Retrospective Analysis for Research and Applications, Version 2 (MERRA-2, Gelaro et al., 2017) data for June and July 2018 (not shown) indicates that the regional precipitation rate was approximately neutral (compared to the climatology). RAPID-CAST occurred during a weak La Nina/ENSO neutral period amid similar regional dust patterns to 2015 (during which an extreme drought occurred in the Caribbean) as indicated from MODIS data and MERRA-2 reanalysis (not shown). We therefore cannot say that the land cover change alone altered surface/atmospheric conditions in the RAMS simulations.

In the context of the aforementioned large-scale conditions, Hurricane Maria significantly impacted the surface-atmosphere exchanges of heat and water vapor across Puerto Rico. These effects are attributed to the replacement of trees by grass and bare soil, which increases transpiration and evaporation as the capacity to hold water is reduced (Mazzacavallo & Kulmatiski, 2015). Hence, much of the available energy was redistributed as latent heat flux. As long as the soil is wet and above the wilting point, it is reasonable to expect higher latent heat flux; however, during dry down periods when conditions are reversed, the sensible heat flux could potentially dominate (Gu et al., 2006). Latent heat increased at several parts of the island at the expense of sensible heat, which increases the overall EF (postMaria). While the reduction in sensible heat potentially lowers the near surface temperature in the wake of the hurricane damage, the increase in latent heat will lead to increased humidity. In addition, the peak liquid water buoyancy values (Figure 8) are higher in the preMaria case (12:00–13:00 AST). At some locations along the Cordillera Central slopes the latent heat flux doubled compared to the preMaria scenario. However, the postMaria case produces higher liquid buoyancy after 14:00 AST on the Cordillera Central and on the west coast (15:00–16:00 AST), resulting in a "+−+−" pattern. The change in surface energy partitioning will directly impact cloud formation. The background flow, in conjunction with local latent heat, evapotranspiration, and thermodynamic variation regulates moist instability over nonuniform terrain (Kirshbaum et al., 2018). If the sensible heat does not increase, enhancement of latent heat flux will reduce the Bowen ratio (ratio of sensible to latent heat flux), impacting local convective rainfall mechanisms.

Therefore, the diminished forest cover adjusts the land surface water and energy exchanges (sensible heat, latent heat, buoyancy, and EF), which when modified in convective (mechanical and thermal) hotspots may impact local rainfall production. These changes modify the moisture transported (sea breeze and orographic lift) at coastal and mountainous regions and alter local boundary layer dynamics as reductions in the Bowen ratio will lead to shallow boundary layers. This could have important implications with regards to precipitation dynamics, as decreases in the buoyancy of air as a result of land changes competes with latent heat increases postMaria to produce precipitating clouds closer to the surface. Another potential impact of the hurricane induced damage is the increased risk of flash floods and soil erosion. Past work by Lopez et al. (1998) has documented that slopes along the Cordillera Central mountain range are particularly prone to soil erosion.

It should also be noted that the convective differences between pre and postMaria scenarios are negligible in San Juan and along the Southern Coast. This leads to the possibility that changes in the horizontal wind over the study period (convergence modification) may have led to changes in convection over El Yunque and the Western Mountains. Coupled with reduced tree cover (roughness) rainfall off the west coast can be produced further inland (postMaria). Thus, damage to the land cover may lead to significant modification

to the island rainfall, and the June 28, 2018 case endured moderate changes in the rainfall pattern and intensity under a modified land scenario. The preMaria case produces higher rain totals near the west coast and over El Yunque—which could be attributed to increased parcel buoyancy as a result of the land cover change (revisit Figure 8). Lastly, the southern coast which experienced minimal convection indicates near zero differences in precipitation between pre and postMaria cases, supporting the sensible/latent heat (Figures 6 and 7), buoyancy (Figure 8), EF (Figure 9), and vertical wind (Figure 10) results.

The u v wind plots (Figure 12) verify increased convergence at the west coast in the postMaria scenario, which produces rainfall further inland. This westerly sea-breeze is a byproduct of surface heating, and changes in the land-sea surface temperature gradient modify the wind intensity and direction. The surface temperature increase in the preMaria case is not uniform across the whole island, but rather is concentrated in the northwestern quadrant and redirects the sea-breeze off the west coast (18.25°N) to flow toward the lowest pressure (south, southwesterly from 11:00 to 12:00 AST). It also appears that there is stronger orographic uplift at the windward side of the mountains but less convergence over El Yunque in the postMaria case. The precipitation totals, particularly along the northern slopes increased, indicating stronger orographic lift over the Cordillera Central mountains in the postMaria case. Although these precipitation results are promising, very few local rainfall events occurred during the RAPID-CAST campaign and further work is required to clearly establish summer precipitation dynamics under modified land conditions.

5. Summary

We quantified land modification across Puerto Rico due to Hurricane Maria and studied the impact of the changes on surface-atmospheric interactions. A comparison of pre and postMaria land cover created using LANDSAT-8 mosaics showed the extensive damage of the hurricane over the island. Key modifications include extreme forest damage in El Yunque, the northwest, and the central regions (53%–11%), and an increase in pasture/grass from 16% to 26%. An increase in developed land cover is also indicated (14%–17%) and could be attributed to better visibility of the surface from the satellite due to reduced tree cover. These modifications significantly altered surface-atmospheric energy and momentum exchanges critical to island induced convection and precipitation processes. Since much of the forest cover was converted to bare soil (13%–41%) or pasture, noticeable changes in upwelling longwave and shortwave radiation are observed island-wide. The general increase in EF at El Yunque and the Western Mountains is attributed to the replacement of trees by grass.

RAMS numerical experiments conducted with pre and postMaria land cover scenarios for the June 23 to July 2, 2018 period indicate modification of the island-wide surface energy budget. Sensible heat fluxes were significantly altered for both cases during the early afternoon, but less impacted during the late afternoon under the postMaria scenario, whereas latent heat fluxes increased during the whole convective period. These results reveal substantial gains in latent heat flux at the expense of sensible heat. These conditions led to predominately reduced liquid buoyancy in the postMaria case, with a lower atmospheric boundary layer. At some locations along the Cordillera Central, the latent heat doubled. The variability in dynamics due to land cover modification was detected in the vertical winds—all which have changed over the Western Mountains and El Yunque. The unique scenario influenced the rainfall pattern in the simulations, which show observable differences in precipitation pattern and intensity between pre and postMaria cases.

The total accumulated precipitation from the June 28, 2018 RAMS simulations show the highest rainfall totals along the center of the island. The preMaria land cover case produces higher rain totals near the western coast, and over El Yunque which could be attributed to increased parcel buoyancy as a result of the land cover change (revisit Figure 8). In addition, changes in the local convective processes are responsible for modifications in rainfall totals and distribution; the orographic effect occurs at El Yunque as well as at the Western Mountains, while the Western Mountains are also impacted by sea breeze/easterly convergence. The highest deviations between postminus preMaria totals (Figure 11d) occur over the Western Mountains while reduced changes are identified over the eastern side of the island. The hourly u v wind evolution indicates westerly oriented sea breeze by 11:00 AST in the postMaria case, attributed to increased convergence which produces rainfall further inland, and stronger orographic uplift at the windward side of the Western Mountains, with less convergence over El Yunque. While these results are promising, additional analyses

of similar localized events are needed to establish the dominant factors and mechanisms that induce these changes in post hurricane environments. Our planned future work includes investigation of hurricane induced land modification on solely localized precipitation events over the summer period. Lastly, this work highlights the need for continuous monitoring of tropical environments after natural disasters as the land cover recovers. This would provide vital information for the improvement of weather forecasting, emergency response, climate prediction, ecosystem services, and governance.

Data Availability Statement

CAST data is available at http://cuerg.ccny.cuny.edu/cast.

References

Angeles, M. E., González, J. E., Ramírez-Beltrán, N. D., Tepley, C. A., & Comarazamy, D. E. (2010). Origins of the Caribbean rainfall bimodal behavior. *Journal of Geophysical Research*, *115*(D11), D11106. https://doi.org/10.1029/2009JD012990

Ayala-Silva, T., & Twumasi, Y. (2004). Hurricane Georges and vegetation change in Puerto Rico using AVHRR satellite data. *International Journal of Remote Sensing*, *25*(9), 1629–1640. https://doi.org/10.1080/01431160310001595037

Bender, M., Knutson, T., Tuleya, R., Sirutis, J., Vecchi, G., Garner, S., & Held, I. (2010). Modeled impact of anthropogenic warming on the frequency of intense Atlantic hurricanes. *Science*, *327*(5964), 454–458. https://doi.org/10.1126/science.1180568

Bennett, S. P., & Mojica, R. (2008). *Hurricane Georges preliminary storm report*, San Juan, Puerto Rico: National Weather Service. Retrieved from https://web.archive.org/web/20081014181517/http://www.srh.noaa.gov/sju/public_report.html

Boose, E. R., Foster, D. R., & Fluet, M. (1994). Hurricane impacts to tropical and temperate forest landscapes. *Ecological Monographs*, *64*(4), 369–440.

Chambers, J. Q., Fisher, J., Zeng, H., Chapman, E., Baker, D., & Hurtt, G. (2007). Hurricane Katrina's carbon footprint on U.S. Gulf Coast forests. *Science*, *318*(5853), 1107. https://doi.org/10.1126/science.1148913

Charlery, J., Nurse, L., & Whitehall, K. (2006). Exploring the relationship between the North Atlantic oscillation and rainfall patterns in Barbados. *International Journal of Climatology*, *26*(6), 819–827. https://doi.org/10.1002/joc.1334

Comarazamy, D. E., & González, J. E. (2011). Regional long-term climate change (1950–2000) in the mid tropical Atlantic and its impacts on the hydrological cycle of Puerto Rico. *Journal of Geophysical Research*, *116*(D21). https://doi.org/10.1029/2010JD015414

Comarazamy, D. E., Gonzalez, J. E., Luvall, J. C., Rickman, D. L., & Bornstein, R. D. (2013). Climate impacts of land-cover and land-use changes in tropical islands under conditions of global climate change. *Journal of Climate*, *26*(5), 1535–1550. https://doi.org/10.1175/JCLI-D-12-00087.1

Cotton, W. R., Pielke, R. A., Sr., Walko, R. L., Liston, G. E., Tremback, C. J., Jiang, H., et al. (2003). RAMS 2001: Current status and future directions. *Meteorology and Atmospheric Physics*, *82*(1), 5–29. https://doi.org/10.1007/s00703-001-0584-9

Feng, Y., Negron-Juarez, R., Patricola, C., Collins, W., Uriarte, M., Hall, J., et al. (2018). Rapid remote sensing assessment of impacts from Hurricane Maria on forests of Puerto Rico. *PeerJ Preprints*, *6*. e26597v1. https://doi.org/10.7287/peerj.preprints.26597v1

Flynn, D. F., Uriarte, M., Crk, T., Pascarella, J. B., Zimmerman, J. K., Aide, T. M., & Caraballo Ortiz, M. A. (2018). Hurricane disturbance alters secondary forest recovery in Puerto Rico. *Biotropica*, *42*(4), 149–157. https://doi.org/10.1111/j.1744-7429.2009.00581.x

Gamble, D. W., & Curtis, S. (2008). Caribbean precipitation: Review, model, and prospect. *Progress in Physical Geography*, *32*(3), 265–276. https://doi.org/10.1177/0309133308096027

Gamble, D. W., Parnell, D. B., & Curtis, S. (2008). Spatial variability of the Caribbean mid-summer drought and relation to north Atlantic high circulation. *International Journal of Climatology*, *28*(3), 343–350. https://doi.org/10.1002/joc.1600

Gelaro, R., McCarty, W., Suárez, M. J., Todling, R., Molod, A., Takacs, L., et al. (2017). The modern-era retrospective analysis for research and applications, version 2 (MERRA-2). *Journal of Climate*, *30*(14), 5419–5454. https://doi.org/10.1175/JCLI-D-16-0758.1

Gu, L., Meyers, T., Pallardy, S. G., Hanson, P. J., Yang, B., Heuer, M., et al. (2006). Direct and indirect effects of atmospheric conditions and soil moisture on surface energy partitioning revealed by a prolonged drought at a temperate forest site. *Journal of Geophysical Research*, *111*(D16), D16102. https://doi.org/10.1029/2006JD007161

Harrington, J. Y. (1997). *The effects of radiative and microphysical processes on simulated warm and transition season Arctic stratus* (Ph.D. dissertation, Atmospheric Science Paper No. 637, p. 289). Fort Collins, Colorado: Colorado State University.

Helmer, E. H., Ramos, O., López, T., Del, M., Quiñones, M., & Diaz, W. (2002). Mapping the forest type and land cover of Puerto Rico, a component of the Caribbean biodiversity hotspot. *Caribbean Journal of Science*, *38*(3–4), 165–183.

Hernández-Ayala, J. (2019). Atmospheric teleconnections and their effects on the annual and seasonal rainfall climatology of Puerto Rico. *Theoretical and Applied Climatology*, *137*(3–4), 2915–2925. https://doi.org/10.1007/s00704-019-02774-3

Homer, C., Huang, C., Yang, L., Wylie, B., & Coan, M. (2004). Development of a 2001 national land cover database for the United States. *Photogrammetric Engineering and Remote Sensing*, *70*(7), 829–840. https://doi.org/10.14358/PERS.70.7.829

Hosannah, N., González, J. E., Lunger, C., & Niyogi, D. (2019). Impacts of local convective processes on rain on the Caribbean Island of Puerto Rico. *Journal of Geophysical Research: Atmospheres*, *124*(12). https://doi.org/10.1029/2018JD029825

Hosannah, N., González, J. E., Rodriguez-Solis, R., Parsiani, H., Moshary, F., Aponte, L., et al. (2017). The Convection, Aerosol, and Synoptic-Effects in the Tropics (CAST) Experiment: Building an understanding of multi-scale impacts on Caribbean weather via field campaigns. *Bulletin of the American Meteorological Society*, *98*(8), 1593–1600. http://dx.doi.org/10.1175/BAMS-D-16-0192.1

Hu, T., & Smith, R. B. (2018). The impact of Hurricane Maria on the vegetation of Dominica and Puerto Rico using multispectral remote sensing. *Remote Sensing*, *10*(6), 827. https://doi.org/10.3390/rs10060827

Imbert, D., & Portecop, J. (2008). Hurricane disturbance and forest resilience: Assessing structural vs. functional changes in a Caribbean dry forest. *Forest Ecology and Management*, *255*(8-9), 3494–3501. https://doi.org/10.1016/j.foreco.2008.02.030

Jury, M. R. (2009). An intercomparison of observational, reanalysis, satellite, and coupled model data on mean rainfall in the Caribbean. *Journal of Hydrometeorology*, *10*(2), 413–430. https://doi.org/10.1175/2008JHM1054.1

Jury, M. R., Chiao, S., & Cécé, R. (2019). The Intensification of Hurricane Maria 2017 in the Antilles. *Atmosphere*, *10*(10), 590. https://doi.org/10.3390/atmos10100590

Jury, M. R., Chiao, S., & Harmsen, E. W. (2009). Mesoscale structure of trade wind convection over Puerto Rico: Composite observations and numerical simulation. *Boundary-Layer Meteorology*, *132*(2), 289–313.

Kang, N., & Elsner, J. (2015). Trade-off between intensity and frequency of global tropical cyclones. *Nature Climate Change*, *5*(7), 661–664. https://doi.org/10.1038/nclimate2646

Kennaway, T., & Helmer, E. H. (2007). The forest types and ages cleared for land development in Puerto Rico. *GIScience & Remote Sensing*, *44*(4), 356–382. https://doi.org/10.2747/1548-1603.44.4.356

Kirshbaum, D. J., Adler, B., Kalthoff, N., Barthlott, C., & Serafin, S. (2018). Moist orographic convection: Physical mechanisms and links to surface-exchange processes. *Atmosphere*, *9*(3), 80. https://doi.org/10.3390/atmos9030080

Kishore, N., Marqués, D., Mahmud, A., Kiang, M. V., Rodriguez, I., Fuller, A., et al. (2018). Mortality in Puerto Rico after Hurricane Maria. *New England Journal of Medicine*, *379*(2), 162–170. https://doi.org/10.1056/NEJMsa1803972

Knutson, T., Camargo, S. J., Chan, J. C., Emanuel, K., Ho, C., Kossin, J., et al. (2019). Tropical cyclones and climate change assessment: Part I: Detection and attribution. *Bulletin of the American Meteorological Society*, *100*(10), 1987–2007. https://doi.org/10.1175/BAMS-D-18-0189.1

Knutson, T., Camargo, S. J., Chan, J. C., Emanuel, K., Ho, C., Kossin, J., et al. (2020). Tropical cyclones and climate change assessment: Part II: Projected response to anthropogenic warming. *Bulletin of the American Meteorological Society*, *101*(3), E303–E322. https://doi.org/10.1175/BAMS-D-18-0194.1

Knutson, T. R., Sirutis, J. J., Vecchi, G. A., Garner, S., Zhao, M., Kim, H., et al. (2013). Dynamical downscaling projections of twenty-first-century Atlantic hurricane activity: CMIP3 and CMIP5 model-based scenarios. *Journal of Climate*, *26*(17), 6591–6617. https://doi.org/10.1175/JCLI-D-12-00539.1

Kok, K., & Winograd, M. (2002). Modelling land-use change for Central America, with special reference to the impact of hurricane Mitch. *Ecological Modelling*, *149*(1-2), 53–69. https://doi.org/10.1016/S0304-3800(01)00514-2

Laing, A. G. (2004). Cases of heavy precipitation and flash floods in the Caribbean during El Niño winters. *Journal of Hydrometeorology*, *5*(4), 577–594. https://doi.org/10.1175/1525-7541

Lawrence, M. B., & Cobb, H. D. (2005). *Hurricane Jeanne tropical cyclone report*, Miami, Florida: National Hurricane Center. Retrieved from http://www.nhc.noaa.gov/data/tcr/AL112004_Jeanne.pdf

Liu, X., Zeng, X., Zou, X., González, G., Wang, C., & Yang, S. (2018). Litterfall production prior to and during hurricanes Irma and Maria in four Puerto Rican forests. *Forests*, *9*(6), 367–383. https://doi.org/10.3390/f9060367

Lopez, T. M., Aide, T. M., & Scatena, F. N. (1998). The effect of land use on soil erosion in the Guadiana watershed in Puerto Rico. *Caribbean Journal of Science*, *34*(3–4), 298–307.

Mazzacavallo, M. G., & Kulmatiski, A. (2015). Modelling water uptake provides a new perspective on grass and tree coexistence. *PloS One*, *10*(12), e0144300. https://doi.org/10.1371/journal.pone.0144300

Milken Institute (2018). *Ascertainment of the estimated excess mortality from Hurricane Maria in Puerto Rico*, Washington, DC: George Washington University. Retrieved from https://prstudy.publichealth.gwu.edu/

Miller, P. W., Kumar, A., Mote, T. L., Moraes, F. D. S., & Mishra, D. R. (2019a). Persistent hydrological consequences of Hurricane Maria in Puerto Rico. *Geophysical Research Letters*, *46*, 1413–1422. https://doi.org/10.1029/2018GL081591

Miller, P. W., Mote, T. L., Kumar, A., & Mishra, D. R. (2019b). Systematic precipitation redistribution following a strong hurricane landfall. *Theoretical and Applied Climatology*, *139*(3-4), 861–872. https://doi.org/10.1007/s00704-019-03000-w

Molinari, J. (1985). A general form of Kuo's cumulus parameterization. *Monthly Weather Review*, *113*, 1411–1416.

National Center for Environmental Prediction (2019). *Cold and warm episodes by season*. College Park, Maryland: National Center for Environmental Prediction. Retrieved from https://origin.cpc.ncep.noaa.gov/products/analysis_monitoring/ensostuff/ONI_v5.php

National Centers for Environmental Prediction/National Weather Service/NOAA/U.S. Department of Commerce (2000). *NCEP FNL Operational Model Global Tropospheric Analyses, continuing from July 1999*. Boulder, CO: Research Data Archive at the National Center for Atmospheric Research, Computational and Information Systems Laboratory. Retrieved from https://doi.org/10.5065/D6M043C6

Negrón-Juárez, R. I. N., Chambers, J. Q., Zeng, H., & Baker, D. B. (2008). Hurricane driven changes in land cover create biogeophysical climate feedbacks. *Geophysical Research Letters*, *35*(23), L23401. https://doi.org/10.1029/2008GL035683

NWS (2016). *ENSO effects across the Caribbean*, San Juan, Puerto Rico: National Weather Service. Retrieved from https://www.weather.gov/sju/climo_enso

Pielke, R. A., Cotton, W. R., Walko, R. L., Tremback, C. J., Lyons, W. A., Grasso, L. D., et al. (1992). A comprehensive meteorological modeling system-RAMS. *Meteorology and Atmospheric Physics, 49*(1), 69–91.

PRB (2016). *2016 World population data sheet* (p. 22). Washington DC: Population Reference Bureau. Retrieved from http://www.prb.org/pdf16/prb-wpds2016-web-2016.pdf

Saleeby, S. M., & van den Heever, S. C. (2013). Developments in the CSU-RAMS aerosol model: Emissions, nucleation, regeneration, deposition, and radiation. *Journal of Applied Meteorology and Climatology*, *52*(12), 2601–2622. https://doi.org/10.1175/JAMC-D-12-0312.1

Schladebeck, J. (2017). *Puerto Rico death toll from Hurricane Maria climbs to 45*, New York, NY: New York Daily News. Retrieved from http://www.nydailynews.com/news/world/puerto-rico-death-toll-hurricane-maria-climbs-45-article-1.3556878

Tang, B. H., & Neelin, J. D. (2004). ENSO influence on Atlantic hurricanes via tropospheric warming. *Geophysical Research Letters*, *31*(24), L24204. https://doi.org/10.1029/2004GL021072

Tanner, E. V. J., Kapos, V., & Healey, J. R. (1991). Hurricane effects on forest ecosystems in the Caribbean. *Biotropica*, *23*(4), 513–521.

Torres-Valcárcel, A. R. (2018). Teleconnections between ENSO and rainfall and drought in Puerto Rico. *International Journal of Climatology*, *38*(S1), e1190–e1204. https://doi.org/10.1002/joc.5444

Tremback, C. J. (1990). *Numerical simulation of a mesoscale convective complex: Model development and numerical results* (Ph.D. Dissertation, Atmospheric Science Paper No. 465). Fort Collins, CO: Colorado State University, Department of Atmospheric Science.

Weaver, P., & Murphy, P. (1990). Forest structure and productivity in Puerto Rico's Luquillo Mountains. *Biotropica*, *22*(1), 69–82. https://doi.org/10.2307/2388721

Zhu, Z., Wang, S., & Woodcock, C. E. (2015). Improvement and expansion of the Fmask algorithm: Cloud, cloud shadow, and snow detection for Landsats 4–7, 8, and Sentinel 2 images. *Remote Sensing of Environment*, *159*, 269–277. https://doi.org/10.1016/j.rse.2014.12.014